

Review

# Review of the 1<sup>st</sup> EUV Light Sources Code Comparison Workshop

John Sheil <sup>1,2,\*</sup> , Oscar Versolato <sup>1,2</sup>, Vivek Bakshi <sup>3</sup> and Howard Scott <sup>4</sup>

<sup>1</sup> Advanced Research Center for Nanolithography, Science Park 106, 1098 XG Amsterdam, The Netherlands

<sup>2</sup> Department of Physics and Astronomy, and LaserLaB, Vrije Universiteit Amsterdam, De Boelelaan 1081, 1081 HV Amsterdam, The Netherlands

<sup>3</sup> EUV Litho, Inc., 10202 Wommack Road, Austin, TX 78748, USA

<sup>4</sup> Lawrence Livermore National Laboratory, Livermore, CA 94551, USA

\* Correspondence: j.sheil@arcnl.nl

**Abstract:** We review the results of the 1<sup>st</sup> Extreme Ultraviolet (EUV) Light Sources Code Comparison Workshop. The goal of this workshop was to provide a platform for specialists in EUV light source plasma modeling to benchmark and validate their numerical codes using well-defined case studies. Detailed consideration of a plethora of atomic collisional and radiative processes is required for modeling EUV light source plasmas. Eight institutions spanning four countries contributed data to the workshop. Two topics were addressed, namely (i) the atomic kinetics and radiative properties of tin plasmas under EUV-generating conditions and (ii) laser absorption in a fully ionized, one-dimensional hydrogen plasma. In this paper, we summarize the key findings of the workshop and outline plans for future iterations of the code comparison activity.

**Keywords:** EUV source plasma; code comparison; atomic kinetics; laser absorption



**Citation:** Sheil, J.; Versolato, O.; Bakshi, V.; Scott, H. Review of the 1<sup>st</sup> EUV Light Sources Code Comparison Workshop. *Atoms* **2023**, *11*, 130. <https://doi.org/10.3390/atoms11100130>

Academic Editors: Lalita Sharma and Jean-Christophe Pain

Received: 25 August 2023

Revised: 26 September 2023

Accepted: 10 October 2023

Published: 13 October 2023



**Copyright:** © 2023 by the authors. Licensee MDPI, Basel, Switzerland. This article is an open access article distributed under the terms and conditions of the Creative Commons Attribution (CC BY) license (<https://creativecommons.org/licenses/by/4.0/>).

## 1. Introduction

The spectroscopic diagnosis and theoretical modeling of plasmas containing heavy, moderately charged ions are very challenging tasks, requiring detailed information on atomic collisional and radiative processes. Such information is key, for instance, in the field of indirect-drive inertial confinement fusion (ICF) research [1–3], where high-energy X-ray radiation generated in a multi-laser-driven gold ( $Z = 79$ ) hohlraum plasma drives the compression of a deuterium-tritium-filled capsule to fusion conditions. Crucial for the design and interpretation of indirect-drive ICF experiments (or any laser-driven high- $Z$  plasma for that matter) is a comprehensive understanding of (i) the interaction of high-intensity laser light with the plasma and (ii) the radiative properties of complex, high- $Z$  ions embedded in a plasma out of equilibrium, a so-called non-local thermodynamic equilibrium (non-LTE) plasma [4]. The predictive capabilities of ICF simulations are, however, often constrained by the approximations (and limitations) of the physical models implemented in the codes, such as the treatment of non-LTE atomic kinetics, radiation transport, laser light absorption, etc. Adequate benchmarking of each of these aspects, be it through experimental comparisons [5,6] or code comparison efforts [7–9], is crucial for ensuring that their coupling in a multi-physics simulation yields reliable results.

Detailed knowledge of fundamental atomic-plasma processes is also crucial for understanding extreme ultraviolet (EUV) plasma light sources for next-generation nanolithography [10–12]. In EUV lithography (EUVL), laser-driven tin plasmas generate intense bursts of EUV radiation that are used to pattern nanometre-scale features on integrated circuits [13,14]. Under optimum experimental conditions, EUV emission from such plasmas comprises an intense, narrowband feature (full width at half maximum  $\approx 0.6$  nm [15]) centered near a wavelength of 13.5 nm. Importantly, only a small fraction of the total emission ( $13.5 \pm 0.135$  nm—the so-called “in-band” region where molybdenum/silicon multilayer

mirrors exhibit high reflectance [16]) is utilized in the patterning process. To date, plasma modeling has played an important role in guiding EUV light source development efforts. Examples include the elucidation of EUV generation in laser-driven tin plasmas [17–23], the characterization of tin-plasma properties [24–30] as well as the identification of experimental conditions (laser parameters, tin target structures, etc.) that optimize the working conditions of the light source [31–36]. Looking to the future and the need to develop more powerful EUV sources (beyond the current 250 W of in-band EUV power [37]) will require (i) new, fundamental insights on EUV generation from complex target structures [34] and (ii) exploring the plasma physics implications of alternate drive-laser concepts, e.g., the use of a Thulium-based 2- $\mu\text{m}$ -wavelength drive laser [38–42].

The task of modeling an EUV light source, which entails simulating laser interaction with a mid- $Z$ , strongly radiating plasma, has many aspects in common with multi-physics ICF simulations. For one, non-LTE atomic kinetics and radiation transport play a crucial role in shaping the observed spectra. Although many codes have been developed for simulating EUV sources, they typically differ in their treatment of the underlying physical processes, e.g., the radiative properties of the plasma, equation-of-state (EOS) properties, and the absorption and refraction of laser light. A multitude of factors can, therefore, contribute to deviations between codes. Differences often arise, for instance, when quantifying the so-called “conversion efficiency” of the light source (the ratio of in-band EUV energy emitted in the  $2\pi$  hemisphere back towards the laser to the laser energy [43]). This metric exhibits a heightened sensitivity to the accuracy of the radiative data (line positions and intensities) used in a simulation. Extensive benchmarking of the various physics components entering such codes is essential for developing a predictive plasma modeling toolkit. Although code-to-code benchmarking has been active in the ICF community for several years [8,9,44–46], no such platform exists for the EUV light source plasma community.

In this paper, we summarize the findings of the 1<sup>st</sup> EUV Light Sources Code Comparison Workshop, which was held at the 2020 Source Workshop [47] (jointly organized by EUV Litho, Inc., the Paul Scherrer Institute and ETH Zürich). The goal of the workshop was to provide a platform for the EUV light source plasma modeling community to test and benchmark their codes using well-defined test problems. In this first edition of the workshop, two aspects of EUV light source plasma modeling were addressed. The first case study investigated the atomic kinetics and radiative properties of tin plasmas under EUV-generating conditions. The second case study examined laser absorption in a one-dimensional, fully-ionized hydrogen plasma. The present paper is structured as follows: In Section 2, we describe the workshop structure and organization. This is followed by an overview of the results and key learnings of the atomic kinetics case study (Section 3) and the laser absorption case study (Section 4). In Section 5, we outline plans for future code comparison activities, and the paper is concluded in Section 6.

## 2. Workshop Organization and Structure

The organization and structure of the 1<sup>st</sup> EUV Light Sources Code Comparison Workshop were modeled on the series of highly successful non-LTE code comparison workshops [44–46,48]. Approximately four months prior to the workshop, the authors of this paper gathered to define a series of test problems to be investigated at a code comparison session at the 2020 Source Workshop [47]. The problems were shared with prospective participants in August 2020. After a series of discussions, two independent case studies were defined. The first of these focused on the atomic kinetics and radiative properties (opacities, emissivities) of tin plasmas in EUV source-relevant conditions. This problem closely resembles a “standard” case study at the non-LTE code comparison workshop. The second case study investigated laser absorption in a static, fully ionized, one-dimensional hydrogen plasma. Although this second case study does not represent EUV light source plasma conditions, this problem served as the first basic test of laser absorption routines. Moreover, it will provide a baseline upon which additional layers of complexity can be introduced, such as including non-LTE radiation transfer effects, thermal

conduction, and/or hydrodynamic motion. Contributors were required to submit their results to the workshop committee one week prior to the workshop in a format similar to that used for the non-LTE code comparison workshops.

The first part of the workshop was devoted to code presentations, where the authors of the submissions described their codes and gave a brief overview of their results. Ten submissions were received for the atomic kinetics case study and 4 submissions were received for the laser absorption problem. A list of participating codes and contributors is provided in Table 1. The final two presentations of the session were devoted to summarizing the results of the two case studies. In this paper, we will give an overview of the key findings of the workshop and outline plans for future code comparison activities. As is standard practice in the proceedings of the non-LTE code comparison workshops, the published results are anonymous.

**Table 1.** List of codes and contributors.

Code	Contributors	Institution (Country)
Case study 1: Atomic kinetics		
JATOM [49]	A. Sasaki, K. Nishihara, A. Sunahara	KPSI, ILE, CMUXE (Japan, USA)
ATOMIC [50,51]	J. Colgan	LANL (USA)
THERMOS [52,53]	I. Yu. Vichev, A. D. Solomyannaya, A. S. Grushin, D. A. Kim	KIAM (Russia)
PrismSPECT [54]	I. E. Golovkin	Prism Comp. (USA)
Cretin [55]	H. A. Scott	LLNL (USA)
SEMILLAC [56,57]	Y. Frank	L2X,LLNL (Israel,USA)
Case study 2: Laser absorption		
STAR2D [58,59]	A. Sunahara, K. Nishihara, A. Sasaki	CMUXE, ILE, KPSI (USA, Japan)
RALEF-2D [60,61]	M. M. Basko	KIAM (Russia)
HELIOS [62]	I. E. Golovkin	Prism Comp. (USA)
Cretin [55]	H. A. Scott	LLNL (USA)

### 3. Case Study 1: Atomic Kinetics of Tin Plasmas

The objective of this case study was to investigate the atomic kinetics and radiative properties of zero-dimensional, i.e., optically thin tin plasmas at EUV light source plasma conditions. In total, 25 test cases were defined and specified according to the (i) electron density of the plasma  $n_e$  and (ii) electron temperature  $T_e$ —see Table 2 for a complete list of plasma conditions. The plasmas were considered quasineutral, i.e.,  $n_e = Z^* n_i$  where  $Z^*$  is the average charge state of the plasma and  $n_i$  is the ion density. The ion temperature was specified to be equal to the electron temperature. The test cases do not consider any external radiation field-driven effects, i.e., the radiation temperature  $T_r = 0$  eV for all test cases. The two extreme density cases  $n_e = 10^{19}$  and  $10^{21}$  cm<sup>-3</sup> are of particular relevance for EUV light source plasmas as they correspond to the critical electron densities (the electron densities beyond which laser light does not propagate in the plasma) for CO<sub>2</sub> ( $\lambda_{\text{laser}} = 10.6$  μm) and Nd:YAG laser light ( $\lambda_{\text{laser}} = 1.064$  μm), respectively. For each test case, participants were asked to compute:

- The charge state distribution (CSD) and average charge state  $Z^*$  of the plasma.
- The emission ( $\eta_\lambda$ ) and absorption ( $\alpha_\lambda$ ) coefficients.
- The spectral purity (SP) of the plasma, defined as the ratio of the emissivity in the in-band region  $13.5 \pm 0.135$  nm to the emissivity in the 5–20 nm region, i.e.,  $\text{SP} (\%) = 100 \times \int_{13.365}^{13.635} \eta_\lambda d\lambda / \int_5^{20} \eta_\lambda d\lambda$ .
- The specific internal energy (SIE), defined as  $\text{SIE} = \sum_j E_j n_j$  where the sum runs over all states  $j$  (levels, configurations, etc.) having energy  $E_j$  and population density (simply “population” in the following)  $n_j$ .

- Contributions to the radiative power losses (RPL): bound-bound, bound-free, and free-free transitions.

**Table 2.** Plasma conditions for the atomic kinetics case study.

$n_e$ (cm <sup>-3</sup> )	$T_e$ (eV)
10 <sup>19</sup>	10, 15, 20, 25, 30, 35, 40
10 <sup>20</sup> , 10 <sup>21</sup>	20, 25, 30, 35, 40, 45, 50, 55, 60

In the following, we divide our discussions into three cases according to the electron density:  $n_e = 10^{19}$  cm<sup>-3</sup> (case 1),  $10^{20}$  cm<sup>-3</sup> (case 2) and  $10^{21}$  cm<sup>-3</sup> (case 3).

3.1. Case 1:  $n_e = 10^{19}$  cm<sup>-3</sup>

In Figure 1a we present computations of the average charge state  $Z^*$  of tin plasmas having  $n_e = 10^{19}$  cm<sup>-3</sup> and  $T_e = 10 - 40$  eV. This electron density is of particular relevance for industrial applications as it corresponds to the critical electron density for CO<sub>2</sub> lasers currently used to drive EUV source plasmas for nanolithography [15,63]. The charge state distributions (CSDs) of the  $T_e = 10$  eV and 30 eV plasmas are shown in Figure 1b and c, respectively.

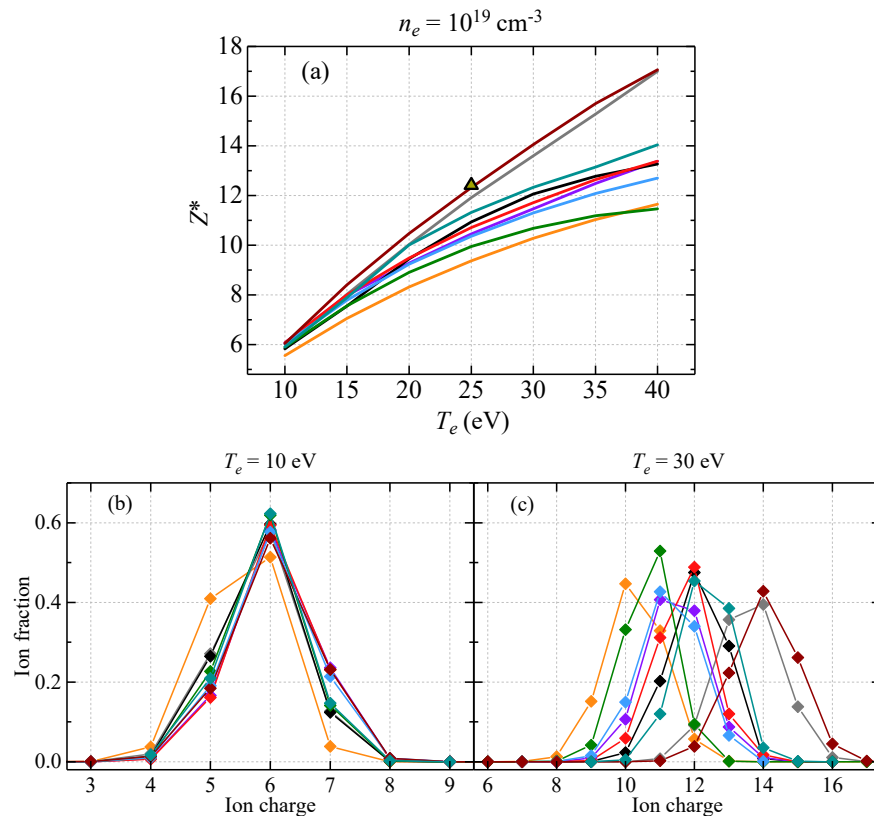


**Figure 1.** (a) Average charge state  $Z^*$  of the plasma as a function of  $T_e$  for  $n_e = 10^{19}$  cm<sup>-3</sup>. Charge state distributions of the (b)  $T_e = 10$  eV and (c)  $T_e = 30$  eV plasmas. The gray and dark red curves, as well as the gold triangle submission, were calculated under the assumption of LTE conditions.

First, for the lowest temperature case ( $T_e = 10$  eV), we see that all codes predict a similar value of  $Z^* \approx 6$ . This convergence in  $Z^*$  is reflected in Figure 1b, where only minor differences in the shapes of the CSDs are observed between most codes. The plasma conditions (high-density, low-temperature) place it close to LTE conditions, and thus, agreement between the codes in this region is expected, as only the atomic structure matters in determining the ionization balance in LTE. With increasing electron temperature,  $Z^*$

increases alongside an increased spread in the various code predictions. This is most apparent for temperatures above 30 eV, where predictions of  $Z^*$  span six charge states. As the electron temperature increases, the plasma moves away from LTE conditions and enters the non-LTE regime, a regime known for producing disagreements among collisional-radiative codes [64]. It should be noted that the calculations shown in gray, dark red, and the single gold triangle (with a black border) were performed under the assumption of LTE conditions. These LTE calculations, which are equivalent to performing Planckian radiation field-driven non-LTE calculations with  $T_r = T_e$ , naturally overestimate the plasma ionicity given that we have specified  $T_r = 0$  eV in the current problem. The spread in  $Z^*$  predictions likely originates from differences in the dielectronic recombination rates, a supposition suggested by investigations undertaken in the non-LTE code comparison workshops [64]. Atomic model completeness, most notably extensive consideration of autoionizing channels, is an important aspect of ionization balance calculations [64,65], which will be addressed in a future iteration of this workshop.

In Figure 2, we present calculations of the spectral purity (SP) of these plasmas. Unlike the  $Z^*$  calculations, no general trend exists among the codes. First, we note that the LTE submissions (gray and dark red curves, gold triangle) predict a peak in the SP for  $T_e = 25$  eV. This plasma condition generates an average charge state  $Z^* \equiv Z_{SP_{peak}}^* \approx 12$  for all three LTE submissions (see Figure 1a). Although the codes agree on  $Z_{SP_{peak}}^*$ , the spread in SP is significant: 30% (dark red curve), 45% (gray curve) and 60% (gold triangle). In Figure 3, we plot the emissivity of the  $T_e = 25$  eV plasma as calculated by the dark red curve and gold triangle submissions. The atomic model associated with the dark red spectrum includes an extensive number of multiply excited states in the atomic structures, and transitions from such states lead to significantly more emission in the 5–13 nm region than for the spectrum shown in gold. This latter spectrum exhibits (i) more intense in-band emission and (ii) less “out-of-band” emission than the dark red spectrum. Both of these factors contribute to the higher spectral purity for the spectrum shown in gold. Returning to Figure 2, we note that the green and orange non-LTE submissions exhibit a steep rise in SP for  $T_e > 20$  eV, where a maximum in the SP is most likely attained for  $T_e > 40$  eV. The blue and bright red submissions, on the contrary, predict a slowly varying SP with temperature, both of which peak for  $Z_{SP_{peak}}^* \approx 11$  (SP = 25% and 10%, respectively). Finally, we note the local SP maximum for the purple curve at  $T_e = 20$  eV is non-physical, arising from a misplaced shifting of spectral lines.

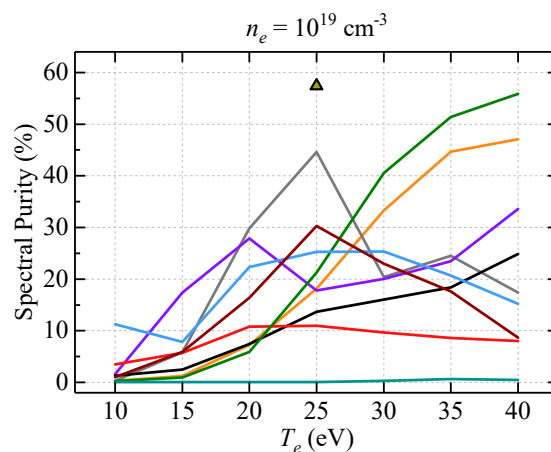


**Figure 2.** Spectral purity as a function of  $T_e$  for  $n_e = 10^{19} \text{ cm}^{-3}$ . The gray and dark red curves, as well as the gold triangle, were calculated under the assumption of LTE conditions.

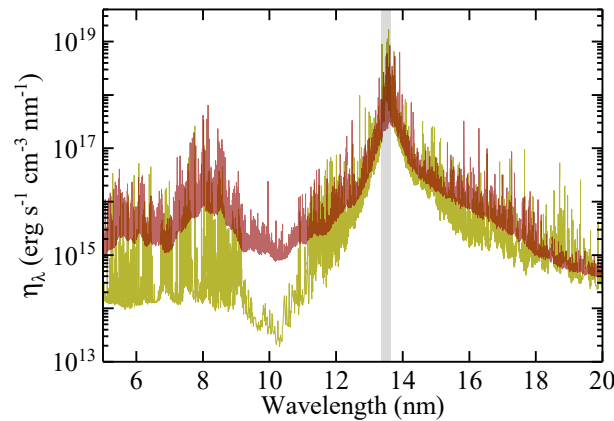


**Figure 3.** Emissivity of a  $n_e = 10^{19} \text{ cm}^{-3}$ ,  $T_e = 25 \text{ eV}$  plasma as calculated by the dark red and gold triangle LTE submissions. The gray shaded area represents the  $13.5 \pm 0.135 \text{ nm}$  in-band region.

The absence of a common trend among the non-LTE submissions shown in Figure 2 is perhaps not too surprising considering (i) the substantial spread in  $Z^*$  predictions for  $T_e > 15 \text{ eV}$  (Figure 1a), (ii) code-to-code variations in the extensivity of the atomic structures and (iii) the rather narrow bandwidth ( $0.27 \text{ nm}$ ) associated with the in-band region. This is exemplified in Figure 4, where we plot the emissivity of plasmas having  $Z^* \approx 11$  for the green, blue, and dark cyan non-LTE submissions ( $T_e = 35, 30$  and  $25 \text{ eV}$  plasmas, respectively). The dark cyan emissivity is clearly very different from that of the green and blue emissivities, the latter of which predicts substantially less in-band emission than the spectrum shown in green. It is well known that the atomic structures of  $\text{Sn}^{10+}$ – $\text{Sn}^{14+}$  ions are subject to strong configuration effects, and this makes their accurate calculation notoriously difficult [20,66]. Extensive benchmarking of these level structures with charge state-specific experimental spectra [67–71] and/or highly accurate ab initio atomic structure calculations [70,72,73] is very much required. Experimental measurements of emission from multiply excited states are also highly desired given their dominant contribution to EUV emission from laser-driven, mid-Z plasmas [23,74,75].

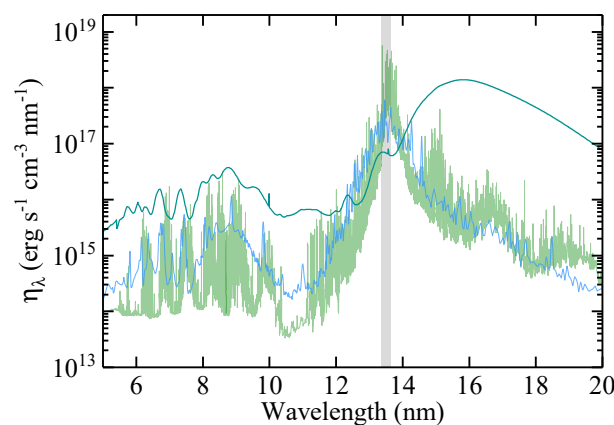


**Figure 4.** Plasma emissivities as calculated by the blue, green, and dark cyan non-LTE submissions for plasmas having  $Z^* \approx 11$ . The gray shaded area represents the  $13.5 \pm 0.135 \text{ nm}$  in-band region.

Finally, in Figure 5 we plot the (a) specific internal energy (SIE) and (b) total radiative power losses (RPL) for the  $n_e = 10^{19} \text{ cm}^{-3}$  plasma as a function of  $T_e$ . The LTE submissions (gray curve, gold triangle) predict a higher SIE than the non-LTE cases. For the submission represented by the green curve, we notice a reduction in the calculated SIE going from  $T_e = 35$  to  $40 \text{ eV}$ . This behavior is rather unusual given the minor change in  $Z^*$  between these two cases, where  $Z^*(T_e = 35 \text{ eV}) \approx 11.2$  and  $Z^*(T_e = 40 \text{ eV}) \approx 11.5$ . Generally

speaking, there is good agreement between the codes for the SIE. Moving to the total RPL, we see that the gray, purple, bright red, and black curves all exhibit a similar “s-like” shape with a near-plateau in the total RPL for  $T_e > 30$  eV.

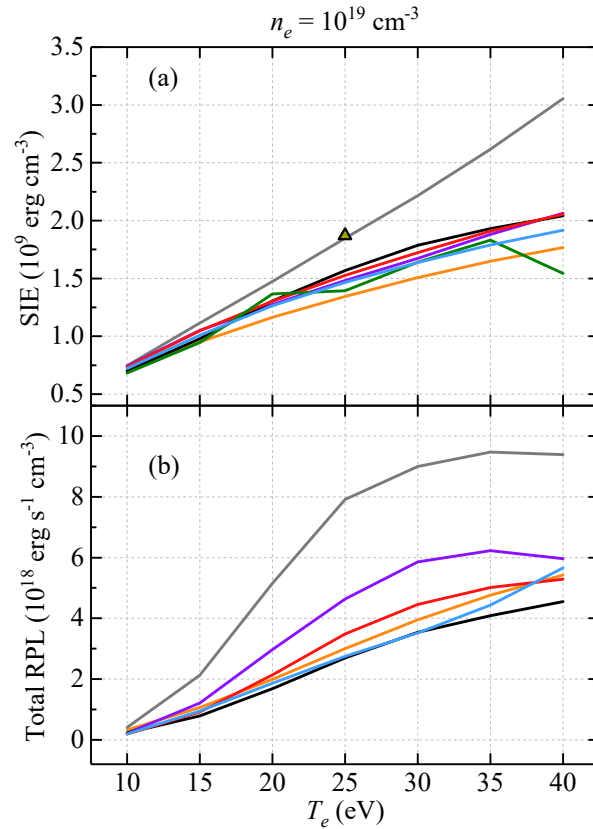


**Figure 5.** (a) Specific internal energy (SIE) and (b) total radiative power losses (RPL) as a function of  $T_e$  for  $n_e = 10^{19} \text{ cm}^{-3}$ . The gray curve and gold triangle submissions were calculated under the assumption of LTE conditions.

### 3.2. Case 2: $n_e = 10^{20} \text{ cm}^{-3}$

In Figure 6a, we plot  $Z^*$  as a function of  $T_e$  for plasmas with  $n_e = 10^{20} \text{ cm}^{-3}$ . As in the  $n_e = 10^{19} \text{ cm}^{-3}$  case, best agreement between  $Z^*$  predictions is achieved for the low temperature ( $T_e = 20/25$  eV) cases. For the highest temperature case ( $T_e = 60$  eV), we see that the majority of the non-LTE submissions are clustered in the  $Z^* = 16$ – $18$  range. The spectral purities calculated by these codes are shown in Figure 6b. Unlike the  $n_e = 10^{19} \text{ cm}^{-3}$  case, we can identify “global” peaks in the spectral purity for the black, purple, green, and orange curves. The average charge state for which the spectral purity peaks,  $Z_{\text{SP peak}}^*$ , is found to be  $Z_{\text{SP peak}}^* \approx 10$  (blue), 10.5 (red and black), 11 (orange), 12 (gray and dark red LTE cases), 13 (green) and 15 (purple). Although the orange curve also exhibits a large SP for  $Z^* \approx 12$ , the spread in  $Z_{\text{SP peak}}^*$  (and SP values) among the various codes is substantial. These observations reinforce the need for extensive benchmarking of atomic spectra calculations and population kinetics models.

The SIE and total RPL as a function of  $T_e$  for  $n_e = 10^{20} \text{ cm}^{-3}$  are shown in Figure 7a and Figure 7b, respectively. First, the order-of-magnitude increase in  $n_e$  ( $10^{19} \text{ cm}^{-3} \rightarrow 10^{20} \text{ cm}^{-3}$ ) yields an order-of-magnitude increase in both the SIE and total RPL. Examining Figure 7a, we note the existence of two local minima in the green curve, one at  $T_e = 35$  eV ( $Z^* \approx 11.9$ ) and the other at  $T_e = 60$  eV ( $Z^* \approx 14.2$ ). Although the exact cause of this behavior is unknown, it may be due to irregularities in the underlying atomic structure. The remaining non-LTE submissions (black, orange, bright red, purple, and blue curves) are in very good agreement with each other across the studied temperature range.

The total RPL curves (excluding that of the bright red submission) exhibit a similar trend; an initial steep rise at low temperatures followed by a near-plateauing in the curve. We note that the purple curve exhibits a peak in the total RPL at  $T_e = 30$  ( $Z^* \approx 11.5$ ).

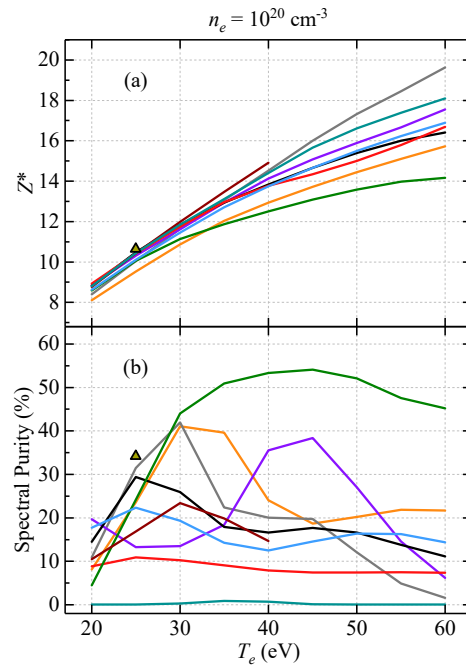


**Figure 6.** (a) Average charge state  $Z^*$  and (b) spectral purity as a function of  $T_e$  for  $n_e = 10^{20} \text{ cm}^{-3}$ . The gray and dark red curves as well as the gold triangle submission were calculated under the assumption of LTE conditions.

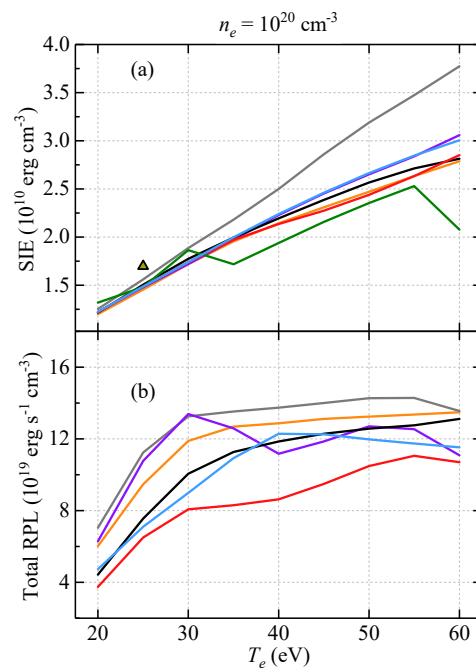


**Figure 7.** (a) Specific internal energy (SIE) and (b) total radiative power losses (RPL) as a function of  $T_e$  for  $n_e = 10^{20} \text{ cm}^{-3}$ . The gray and gold triangle submissions were calculated under the assumption of LTE conditions.

### 3.3. Case 3: $n_e = 10^{21} \text{ cm}^{-3}$

Finally, we discuss the high-density  $n_e = 10^{21} \text{ cm}^{-3}$  case. We show in Figure 8a the average charge state  $Z^*$  and (b) spectral purity for plasmas with  $n_e = 10^{21} \text{ cm}^{-3}$  and

various  $T_e$ . The vast majority of the codes predict similar  $Z^*$  values in the studied  $T_e$  range. In fact, the plasma conditions considered here are close to LTE conditions, and this is the reason for the good agreement between the codes. Examining Figure 8b, we see that the SP curves all exhibit a similar trend to the  $n_e = 10^{20} \text{ cm}^{-3}$  case, however, the maximum SP reached in the  $n_e = 10^{20} \text{ cm}^{-3}$  case is higher than that achieved in the higher-density  $n_e = 10^{21} \text{ cm}^{-3}$  case. To investigate this further, we show in Figure 9 the plasma emissivities as calculated by the green submission for the  $n_e = 10^{20} \text{ cm}^{-3}$ ,  $T_e = 45 \text{ eV}$  case (shown in light green in Figure 9) and the  $n_e = 10^{21} \text{ cm}^{-3}$ ,  $T_e = 45 \text{ eV}$  case (shown in dark green in Figure 9). Both of these plasmas exhibit  $Z^* \approx 13$ . It is clear that the  $n_e = 10^{21} \text{ cm}^{-3}$  spectrum contains more in- and out-of-band emission compared to the  $n_e = 10^{20} \text{ cm}^{-3}$  case. It is also interesting to note the two orders of magnitude difference in emissivity in the 5–10 nm range between both cases. In Figure 10, we plot the (a) SIE and (b) total RPL as a function of  $T_e$  for  $n_e = 10^{21} \text{ cm}^{-3}$ . In general, good agreement is found between the codes for the SIE. In terms of the total RPL, the submissions generally follow the same trend as the  $n_e = 10^{20} \text{ cm}^{-3}$  case. As in the  $n_e = 10^{20} \text{ cm}^{-3}$  case, the purple submission exhibits a peak in the total RPL for  $Z^* \approx 11.5$  ( $T_e = 35 \text{ eV}$ ).

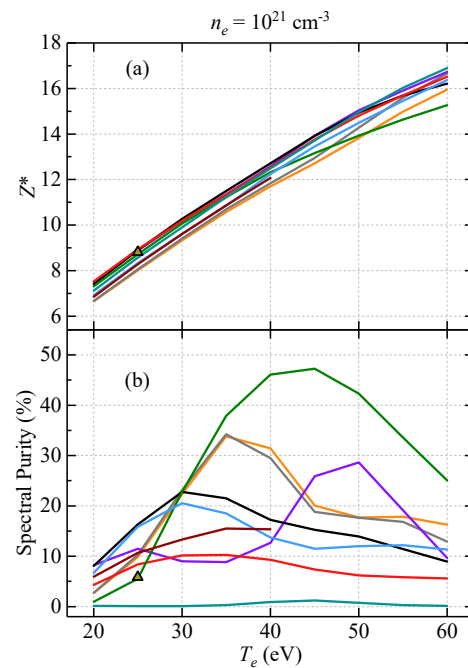


**Figure 8.** (a) Average charge state  $Z^*$  and (b) spectral purity as a function of  $T_e$  for  $n_e = 10^{21} \text{ cm}^{-3}$ . The gray and dark red curves, as well as the gold triangle submission, were calculated under the assumption of LTE conditions.

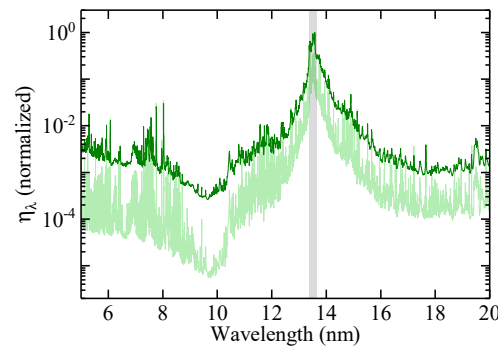


**Figure 9.** Normalized emissivities of the  $T_e = 45 \text{ eV}$ ,  $n_e = 10^{20} \text{ cm}^{-3}$  plasma (light green) and the  $T_e = 45 \text{ eV}$ ,  $n_e = 10^{21} \text{ cm}^{-3}$  (dark green) plasma. The gray shaded area represents the  $13.5 \pm 0.135 \text{ nm}$  in-band region.

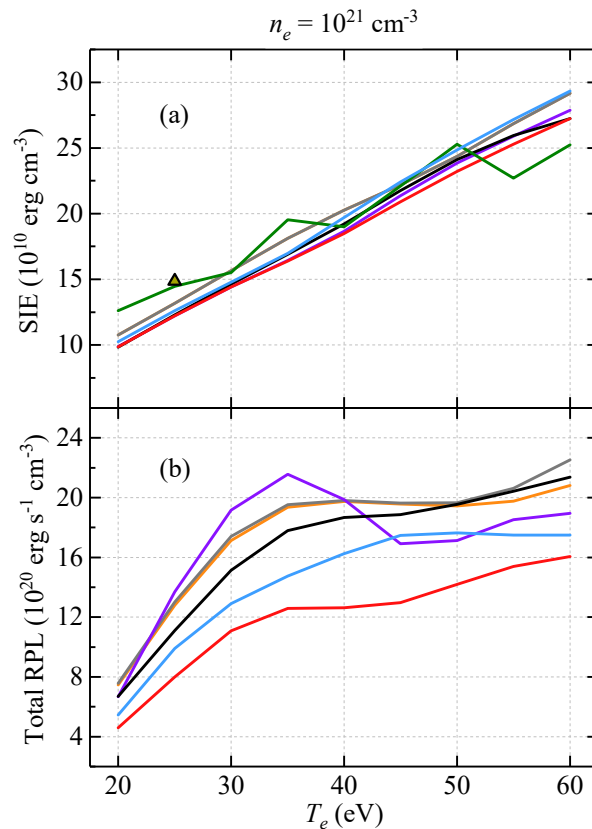


**Figure 10.** (a) Specific internal energy (SIE) and (b) total radiative power losses (RPL) as a function of  $T_e$  for  $n_e = 10^{21} \text{ cm}^{-3}$ . The gray curve and gold triangle submissions were calculated under the assumption of LTE conditions.

#### 4. Case Study 2: Laser Absorption in a Fully Ionized Hydrogen Plasma

We will now examine the second case study addressed at the workshop, that of an investigation of laser absorption in a fully ionized hydrogen plasma. As mentioned in Section 2, this problem served as the first basic test of laser absorption routines used in radiation-hydrodynamic codes. As will be discussed in Section 5, additional layers of complexity will be added to this problem in future iterations of the workshop.

The problem setup is as follows: the plasma has a one-dimensional planar geometry with a computational domain defined over  $x \in [0, 300] \mu\text{m}$ . The spatial mesh consists of 20,000 equally spaced zones over this domain. The plasma parameters (temperature and density) are constant in time and are specified according to

$$n_e = \min\left(10^{22}, \frac{10^{24}}{x^3}\right) \text{cm}^{-3} \tag{1}$$

$$T_e = \max[3, 93y \exp(-y^{1/2})] \text{eV} \tag{2}$$

where  $y = \max(0, x - 8)$ . These profiles are illustrated in Figure 11. As the plasma consists of fully ionized hydrogen, the number density specifies both the electron and ion densities. The laser pulse is incident at  $x = 300 \mu\text{m}$  at normal incidence, and laser absorption was to be modeled using inverse bremsstrahlung. Two laser pulse wavelengths were considered:  $\lambda_{\text{laser}} = 1.064 \mu\text{m}$  (Nd:YAG laser) and  $\lambda_{\text{laser}} = 10.6 \mu\text{m}$  (CO<sub>2</sub> laser). The incident laser intensity is  $10^{11} \text{ W/cm}^2$  for both laser wavelength cases. The plasma is stationary (no hydrodynamic motion) and energy transfer processes such as radiation transport and thermal conduction were not included. The requested quantities include the incident and reflected laser power densities, the deposited laser power, the laser absorption coefficient, and the (electron-ion) Coulomb logarithm.

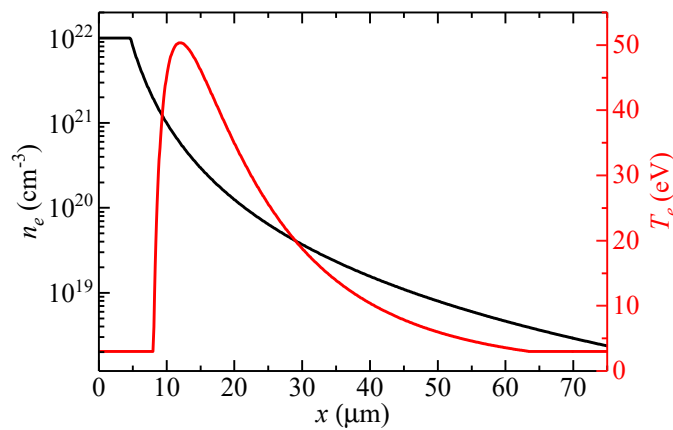


**Figure 11.** Profiles of the electron density  $n_e$  (black) and electron temperature  $T_e$  (red) for  $x \in [0, 75]$   $\mu\text{m}$  in the laser absorption case study. Note that the computational mesh extends to  $x = 300 \mu\text{m}$ .

In Figure 12, we plot the laser power density  $I_{\text{laser}}$  as a function of distance  $x$  for  $\lambda_{\text{laser}} = 1.064 \mu\text{m}$ . The dark solid lines indicate the total laser power density incident on the plasma (indicated by the arrow pointing towards  $x = 0 \mu\text{m}$ ), and the dotted lines represent the power density of the reflected laser light (indicated by the arrow pointing towards  $x = 300 \mu\text{m}$ ). A similar plot for the  $\lambda_{\text{laser}} = 10.6 \mu\text{m}$  case is shown in Figure 13. As expected, the laser light propagates up the critical electron density  $n_{\text{crit}} \approx 10^{21} / \lambda_{\text{laser}}^2$ , which occurs at  $x \approx 10 \mu\text{m}$  for  $\lambda_{\text{laser}} = 1.064 \mu\text{m}$  and  $x \approx 45 \mu\text{m}$  for  $\lambda_{\text{laser}} = 10.6 \mu\text{m}$ . In Figure 14, we plot the laser energy deposition  $E_{\text{dep}}$  for  $\lambda_{\text{laser}} = 1.064 \mu\text{m}$  (solid lines) and  $\lambda_{\text{laser}} = 10.6 \mu\text{m}$  (dashed lines). Good agreement between the codes is observed for both laser wavelength cases. The blue, red, and orange submissions employ a standard ray-tracing approach over the complete path of the laser. The submission shown in green transitions from a ray-tracing approach in the underdense plasma to a wave optics approach near the critical electron density. Here, the 1D Helmholtz equations are solved along the evanescent ray, which propagates beyond the critical electron density, as seen in Figure 14. The “kink” in the  $E_{\text{dep}}$  profiles at  $x \approx 64 \mu\text{m}$  is a remnant of the temperature profile which transitions from the analytic form in Equation (2) to a constant  $T_e = 3 \text{ eV}$  profile for  $x > 64 \mu\text{m}$ . For  $\lambda_{\text{laser}} = 1.064 \mu\text{m}$ , we note an approximate factor of two difference between the blue and green/orange submissions for  $x > 50 \mu\text{m}$ . This is attributed to differences in the Coulomb logarithms calculated by the codes (see next paragraph).

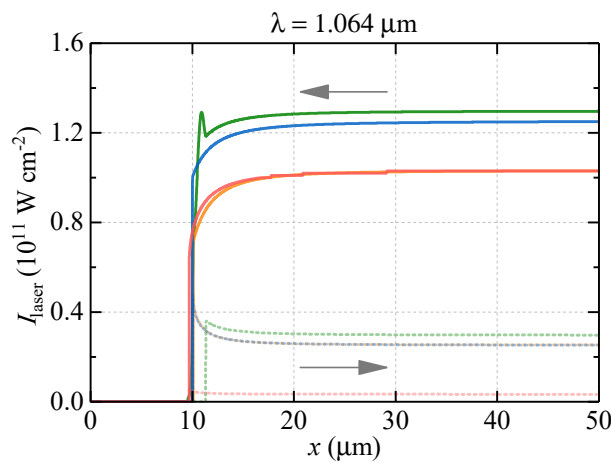


**Figure 12.** Laser power density  $I_{\text{laser}}$  as a function of distance  $x$  for  $\lambda = 1.064 \mu\text{m}$ . Solid lines correspond to the total laser power density. The dotted lines represent the power density of the reflected laser light. The gray arrows indicate the in-going and out-going laser light path.

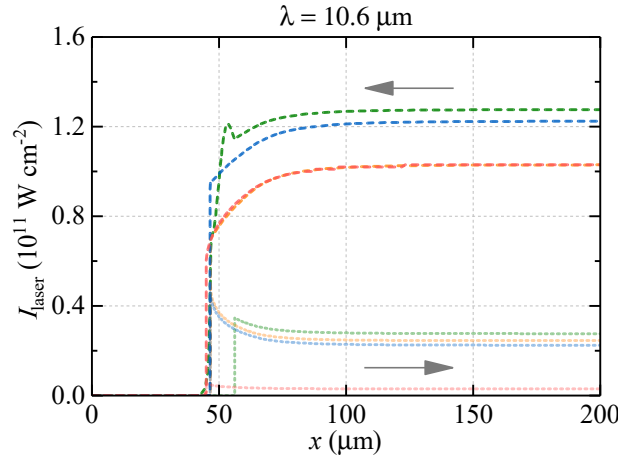


**Figure 13.** Laser power density  $I_{\text{laser}}$  as a function of distance  $x$  for  $\lambda = 10.6 \mu\text{m}$ . The dashed lines correspond to the total laser power density. The dotted lines represent the power density of the reflected laser light. The gray arrows indicate the in-going and out-going laser light path.

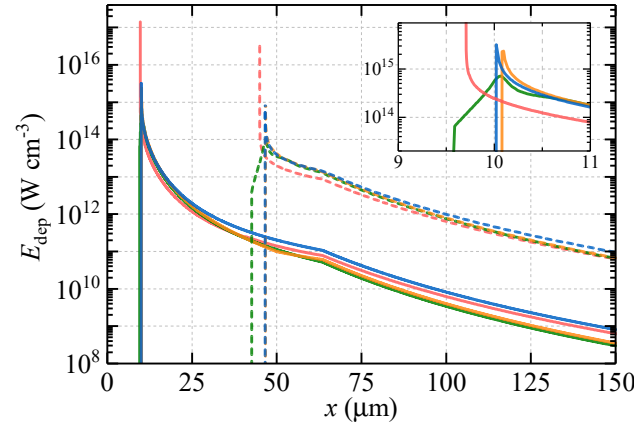


**Figure 14.** Laser energy deposition  $E_{\text{dep}}$  as a function of distance  $x$ . Solid lines correspond to the  $\lambda_{\text{laser}} = 1.064 \mu\text{m}$  case, and the dashed lines correspond to the  $\lambda_{\text{laser}} = 10.6 \mu\text{m}$  case. The inset figure provides a zoomed-in view near the critical density of the  $\lambda_{\text{laser}} = 1.064 \mu\text{m}$  case.

The final two quantities we wish to discuss are the Coulomb logarithm  $\ln(\Lambda)$  and the laser absorption coefficient  $\alpha$ . These quantities are presented for the blue, green, and orange code submissions. In Figure 15, we plot  $\ln(\Lambda)$  as a function of distance  $x$  for the various codes. First, we note that the  $\lambda_{\text{laser}} = 1.064$  and  $10.6 \mu\text{m}$  cases overlap for the blue curve, implying that the approach used to derive  $\ln(\Lambda)$  is independent of laser wavelength. The  $\ln(\Lambda)$  value calculated by the blue submission is based on the formalism of Lee and More [76], where  $\ln(\Lambda) = \frac{1}{2} \ln(1 + b_{\text{max}}^2/b_{\text{min}}^2)$  and  $b_{\text{max}}$  ( $b_{\text{min}}$ ) are the maximum (minimum) impact parameters. In this approach,  $b_{\text{max}} = \max[\lambda_{\text{DH}}, R_0]$ , where  $\lambda_{\text{DH}}$  is the Debye-Hückel screening length and  $R_0 = (4\pi n_i/3)^{-1/3}$  is the average-ion radius.

The calculation of  $\ln(\Lambda)$  for the submission shown in orange is based on the work of Skupsky [77]. Unlike the model of Lee and More, the model of Skupsky explicitly accounts for the laser angular frequency  $\omega$  in the determination of  $b_{\text{max}}$  through  $b_{\text{max}} = \min[\max(\lambda_{\text{DH}}, R_0), v_t/\omega]$ , where  $v_t = (T_e/m_e)^{1/2}$  and  $m_e$  is the electron mass. The value  $b_{\text{max}} = v_t/\omega$  corresponds to the high-frequency (low-density) plasma limit [77]. Although good agreement is observed between the blue and orange submissions for  $x < 64 \mu\text{m}$  in the  $\lambda_{\text{laser}} = 10.6 \mu\text{m}$  case (dashed curves), the orange submission exhibits a much steeper fall-off in  $\ln(\Lambda)$  in the  $15 < x < 50 \mu\text{m}$  range for the  $\lambda_{\text{laser}} = 1.064 \mu\text{m}$  case (solid curves). Importantly, both models require  $\ln(\Lambda) \geq 2$ .

Unlike the blue and orange submissions, the submission shown in green uses an interpolation formula for  $\ln(\Lambda)$ , which enables a smooth transition from the weakly

coupled plasma limit ( $\Lambda \gg 1$ ) to that of solid metals at room temperature ( $\Lambda \ll 1$ ). This approach yields good agreement with the orange submission, especially for the  $\lambda_{\text{laser}} = 10.6 \mu\text{m}$  case. We note that the green submission predicts  $\ln(\Lambda) < 2$  for  $x > 64 \mu\text{m}$  in the  $\lambda_{\text{laser}} = 1.064 \mu\text{m}$  case.

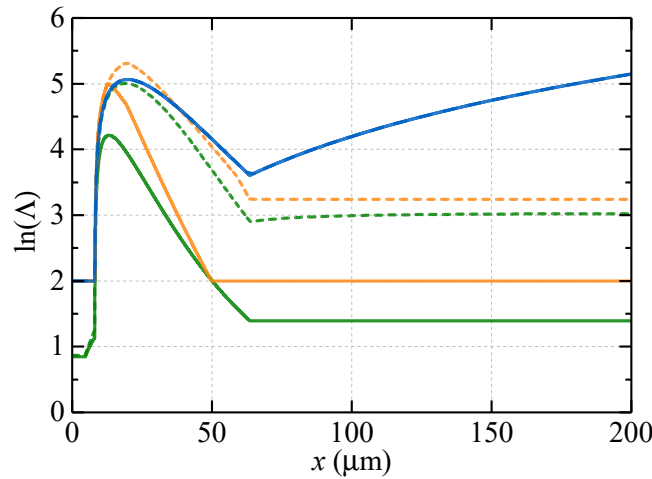


**Figure 15.** Coulomb logarithm  $\ln(\Lambda)$  as a function of distance  $x$ . Solid lines correspond to the  $\lambda = 1.064 \mu\text{m}$  case and dashed lines correspond to  $\lambda = 10.6 \mu\text{m}$ .

Finally, we plot in Figure 16 the laser absorption coefficient  $\alpha$  as a function of distance  $x$  for the  $\lambda_{\text{laser}} = 1.064 \mu\text{m}$  and  $10.6 \mu\text{m}$  laser cases. An approximate form for  $\alpha$  can be written [78]

$$\alpha \approx 900 \left( \frac{n_e}{10^{20}} \right) \left( \frac{n_i}{10^{20}} \right) \frac{(Z^*)^2 (\lambda_{\text{laser}})^2}{(T_e)^{3/2}} \frac{\ln(\Lambda)}{\sqrt{1 - \frac{n_e}{n_c}}} \text{cm}^{-1}, \quad (3)$$

where  $n_c \approx 1.1 \times 10^{21} / (\lambda_{\text{laser}})^2$  is the critical electron density. Good agreement between the codes in underdense plasma regions is observed. The near factor-of-two difference between the green and blue submissions for the  $\lambda_{\text{laser}} = 1.064 \mu\text{m}$  case is attributed to the aforementioned differences in the Coulomb logarithm.

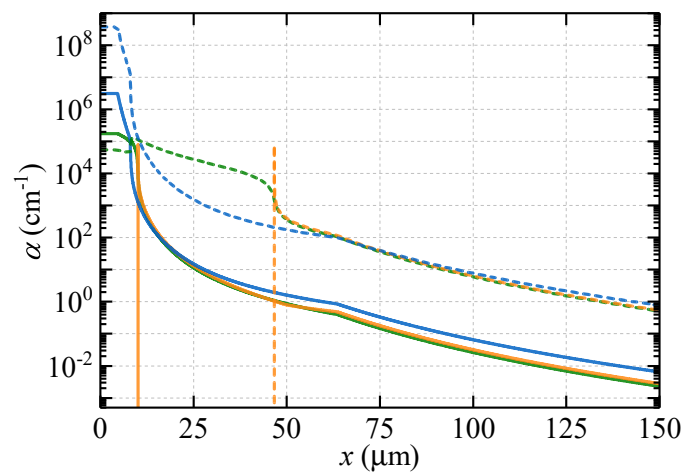


**Figure 16.** Laser absorption coefficient  $\alpha$  as a function of distance  $x$ . Solid lines correspond to the  $\lambda = 1.064 \mu\text{m}$  case and the dashed lines correspond to the  $\lambda = 10.6 \mu\text{m}$  case.

## 5. Discussion and Outlook

The goal of this workshop was to initiate a code comparison activity in the EUV source plasma modeling community. In this respect, the workshop very much served its purpose. For one, the workshop highlighted a surprisingly large spread in predictions of the spectral purity of tin plasmas. This has its origins in the fact that (i) the codes predict different charge state distributions for a given  $T_e$  and (ii) the underlying atomic structures (from which the opacities and emissivities are built) can differ substantially from code-to-code. This has important consequences for radiation-hydrodynamic simulations of EUV sources, which take as input such radiative data to predict the conversion efficiency of laser-plasma EUV sources. These findings call for renewed investigations of tin-ion atomic structures and population kinetics in dense, laser-driven plasmas. Benchmark experiments of the ionization distributions of tin plasmas at EUV-generating conditions would greatly assist the validation and verification of collisional-radiative models.

As a follow-up to this first meeting, a 2<sup>nd</sup> EUV Light Sources Code Comparison Workshop was held on the 25<sup>th</sup> October 2021 (the results of this meeting will be presented in a separate paper). A major development for this second meeting was that the software tools developed for the non-LTE workshops were made available to workshop organizers and participants. This enabled more detailed investigations and comparisons of a huge number of quantities (level populations, ionization rates, recombination rates, etc.) that were not investigated at the first workshop. The atomic kinetics problem was also expanded to study the effects of an external radiation field on population kinetics.

A new case study investigating radiation transport through a uniform tin sphere was defined. The goal of this problem was to obtain a self-consistent radiation field and material properties throughout the sphere. This problem served as an extension of the optically thin atomic kinetics case study, where optical depth effects play an important role in shaping the radiation field. Both steady-state and time-dependent variations of the problem were investigated.

Finally, a time-dependent laser absorption case study was defined. In this problem, participants were asked to model the absorption of  $\lambda_{\text{laser}} = 1.064 \mu\text{m}$  (Nd:YAG),  $1.88 \mu\text{m}$  (Th) and  $10.6 \mu\text{m}$  (CO<sub>2</sub>) laser light in a one-dimensional planar tin plasma. As before, the plasma was assumed to be static (no hydrodynamic motion), and the processes of thermal conduction and radiation transport were omitted. In this way, the plasma could only gain energy through laser absorption and lose energy by radiating. The electron number density of the plasma was to be determined by evolving the ionization balance in time using non-LTE atomic kinetics. With this problem definition, we have edged closer to more “realistic” conditions whilst maintaining some degree of simplicity to ensure insightful comparisons.

## 6. Conclusions

In this paper, we have given an overview of the 1<sup>st</sup> EUV Light Sources Code Comparison Workshop. Two topics were addressed at the workshop. The first of these was an investigation of the atomic kinetics and radiative properties of tin plasmas at EUV-generating conditions. This case study highlighted a significant spread in predictions of the spectral purity of tin plasmas. This calls for renewed investigations of tin-ion atomic structures and plasma population kinetics processes. The second case study investigated laser absorption in a fully ionized, one-dimensional hydrogen plasma, where differences in the underlying Coulomb logarithms were found to be the principal source of disagreement among the codes.

**Author Contributions:** Conceptualization, J.S., O.V., V.B. and H.S.; formal analysis, J.S.; writing—original draft preparation, J.S.; writing—review and editing, J.S., O.V., V.B. and H.S.; visualization, J.S. All authors have read and agreed to the published version of the manuscript.

**Funding:** The work of H. Scott was performed under the auspices of the U. S. Department of Energy by Lawrence Livermore National Laboratory under Contract DE-AC52-07NA27344.

**Data Availability Statement:** Data presented in this paper is available upon reasonable request.

**Acknowledgments:** We would like to thank all workshop participants, without whom this code comparison effort would not have been possible. We would also like to thank S. Langer and H. Frank for discussions during the preparatory stages of the workshop and Y. V. Ralchenko for making the non-LTE workshop software tools available for the 2<sup>nd</sup> EUV source code comparison workshop. Part of this work has been carried out at the Advanced Research Center for Nanolithography (ARCNL), a public-private partnership of the University of Amsterdam (UvA), the Vrije Universiteit Amsterdam (VU), NWO, the semi-conductor equipment manufacturer ASML and associate partner Rijksuniversiteit Groningen (RuG).

**Conflicts of Interest:** The authors declare no conflict of interest.

## References

1. Lindl, J. Development of the indirect-drive approach to inertial confinement fusion and the target physics basis for ignition and gain. *Phys. Plasmas* **1995**, *2*, 3933–4024. [[CrossRef](#)]
2. Kline, J.L.; Batha, S.H.; Benedetti, L.R.; Bennett, D.; Bharkar, S.; Hopkins, L.B.; Biener, J.; Biener, M.M.; Bionta, R.; Bond, E.; et al. Progress of indirect drive inertial confinement fusion in the United States. *Nucl. Fusion* **2019**, *59*, 112018. [[CrossRef](#)]
3. Zylstra, A.B.; Hurricane, O.A.; Callahan, D.A.; Kritcher, A.L.; Ralph, J.E.; Robey, H.F.; Ross, J.S.; Young, C.V.; Baker, K.L.; Casey, D.T.; et al. Burning plasma achieved in inertial fusion. *Nature* **2022**, *601*, 542. [[CrossRef](#)]
4. Ralchenko, Y. (Ed.) *Modern Methods in Collisional-Radiative Modeling of Plasmas*; Springer: Cham, Switzerland, 2016; pp. 81–104.
5. Foord, M.E.; Glenzer, S.H.; Thoe, R.S.; Wong, K.L.; Fournier, K.B.; Wilson, B.G.; Springer, P.T. Ionization Processes and Charge-State Distribution in a Highly Ionized High-Z Laser-Produced Plasma. *Phys. Rev. Lett.* **2000**, *85*, 992–995. [[CrossRef](#)]
6. Heeter, R.F.; Hansen, S.B.; Fournier, K.B.; Foord, M.E.; Froula, D.H.; Mackinnon, A.J.; May, M.J.; Schneider, M.B.; Young, B.K.F. Benchmark Measurements of the Ionization Balance of Non-Local-Thermodynamic-Equilibrium Gold Plasmas. *Phys. Rev. Lett.* **2007**, *99*, 195001. [[CrossRef](#)]
7. Piron, R.; Gilleron, F.; Aglitskiy, Y.; Chung, H.K.; Fontes, C.; Hansen, S.; Marchuk, O.; Scott, H.; Stambulchik, E.; Ralchenko, Y. Review of the 9th NLTE code comparison workshop. *High Energy Density Phys.* **2017**, *23*, 38–47. [[CrossRef](#)] [[PubMed](#)]
8. Gaffney, J.A.; Hu, S.X.; Arnault, P.; Becker, A.; Benedict, L.X.; Boehly, T.R.; Celliers, P.M.; Ceperley, D.M.; Čertík, O.; Clérouin, J.; et al. A Review of Equation-of-State Models for Inertial Confinement Fusion Materials. *High Energy Density Phys.* **2018**, *28*, 7–24. [[CrossRef](#)]
9. Grabowski, P.E.; Hansen, S.B.; Murillo, M.S.; Stanton, L.G.; Graziani, F.R.; Zylstra, A.B.; Baalrud, S.D.; Arnault, P.; Baczewski, A.D.; Benedict, L.X.; et al. Review of the first charged-particle transport coefficient comparison workshop. *High Energy Density Phys.* **2020**, *37*, 100905. [[CrossRef](#)]
10. Bakshi, V. (Ed.) *EUV Sources for Lithography*; SPIE Press: Washington, DC, USA, 2006.
11. O’Sullivan, G.; Li, B.; D’Arcy, R.; Dunne, P.; Hayden, P.; Kilbane, D.; McCormack, T.; Ohashi, H.; O’Reilly, F.; Sheridan, P.; et al. Spectroscopy of highly charged ions and its relevance to EUV and soft X-ray source development. *J. Phys. B* **2015**, *48*, 144025. [[CrossRef](#)]
12. Versolato, O.O. Physics of laser-driven tin plasma sources of EUV radiation for nanolithography. *Plasma Sources Sci. Technol.* **2019**, *28*, 083001. [[CrossRef](#)]
13. Fomenkov, I.; Brandt, D.; Ershov, A.; Schafgans, A.; Tao, Y.; Vaschenko, G.; Rokitski, S.; Kats, M.; Vargas, M.; Purvis, M.; et al. Light sources for high-volume manufacturing EUV lithography: Technology, performance, and power scaling. *Adv. Opt. Technol.* **2017**, *6*, 173–186. [[CrossRef](#)]
14. Felix, N.M.; Attwood, D.T. EUV Lithography Perspective: From the beginning to HVM (Conference Presentation). In Proceedings of the Extreme Ultraviolet (EUV) Lithography XI, San Jose, CA, USA, 24–27 February 2020; Volume 11323.
15. van de Kerkhof, M.A.; Liu, F.; Meeuwissen, M.; Zhang, X.; Bayraktar, M.; de Kruif, R.C.; Davydova, N.V. High-power EUV lithography: Spectral purity and imaging performance. *J. Micro Nanolithogr. MEMS MOEMS* **2020**, *19*, 033801. [[CrossRef](#)]
16. Bajt, S.; Alameda, J.B.; Barbee, T.W., Jr.; Clift, W.M.; Folta, J.A.; Kaufmann, B.; Spiller, E.A. Improved reflectance and stability of Mo-Si multilayers. *Opt. Eng.* **2002**, *41*, 1797–1804. [[CrossRef](#)]
17. White, J.; Hayden, P.; Dunne, P.; Cummings, A.; Murphy, N.; Sheridan, P.; O’Sullivan, G. Simplified modeling of 13.5 nm unresolved transition array emission of a Sn plasma and comparison with experiment. *J. Appl. Phys.* **2005**, *98*, 113301. [[CrossRef](#)]
18. Poirier, M.; Blenski, T.; de Gaufridy de Dortan, F.; Gilleron, F. Modeling of EUV emission from xenon and tin plasma sources for nanolithography. *J. Quant. Spectrosc. Radiat. Transfer* **2006**, *99*, 482–492. [[CrossRef](#)]
19. Novikov, V.G.; Ivanov, V.V.; Koshelev, K.N.; Krivtsov, V.M.; Solomyannaya, A.D. Calculation of tin emission spectra in discharge plasma: The influence of reabsorption in spectral lines. *High Energy Density Phys.* **2007**, *3*, 198–203. [[CrossRef](#)]
20. Koike, F.; Fritzsche, S. Relativistic calculations for highly correlated atomic and highly charged ionic systems. *Radiat. Phys. Chem.* **2007**, *76*, 404–411. [[CrossRef](#)]
21. Sasaki, A.; Sunahara, A.; Nishihara, K.; Nishikawa, T.; Fujima, K.; Kagawa, T.; Koike, F.; Tanuma, H. Atomic modeling of the plasma EUV sources. *High Energy Density Phys.* **2007**, *3*, 250–255. [[CrossRef](#)]

22. Sasaki, A.; Sunahara, A.; Furukawa, H.; Nishihara, K.; Fujioka, S.; Nishikawa, T.; Koike, F.; Ohashi, H.; Tanuma, H. Modeling of radiative properties of Sn plasmas for extreme-ultraviolet source. *J. Appl. Phys.* **2010**, *107*, 113303. [[CrossRef](#)]
23. Torretti, F.; Sheil, J.; Schupp, R.; Basko, M.M.; Bayraktar, M.; Meijer, R.A.; Witte, S.; Ubachs, W.; Hoekstra, R.; Versolato, O.O.; et al. Prominent radiative contributions from multiply-excited states in laser-produced tin plasma for nanolithography. *Nat. Commun.* **2020**, *11*, 2334. [[CrossRef](#)]
24. MacFarlane, J.J.; Rettig, C.L.; Wang, P.; Golovkin, I.E.; Woodruff, P.R. Radiation-hydrodynamics, spectral, and atomic physics modeling of laser-produced plasma EUVL light sources. In Proceedings of the Emerging Lithographic Technologies IX, San Jose, CA, USA, 1–3 March 2005; Volume 5751, pp. 588–600.
25. White, J.; O’Sullivan, G.; Zakharov, S.; Choi, P.; Zakharov, V.; Nishimura, H.; Fujioka, S.; Nishihara, K. Tin laser-produced plasma source modeling at 13.5 nm for extreme ultraviolet lithography. *Appl. Phys. Lett.* **2008**, *92*, 151501. [[CrossRef](#)]
26. Nishihara, K.; Sunahara, A.; Sasaki, A.; Nunami, M.; Tanuma, H.; Fujioka, S.; Shimada, Y.; Fujima, K.; Furukawa, H.; Kato, T.; et al. Plasma physics and radiation hydrodynamics in developing an extreme ultraviolet light source for lithography. *Phys. Plasmas* **2008**, *15*, 056708. [[CrossRef](#)]
27. Basko, M.M.; Novikov, V.G.; Grushin, A.S. On the structure of quasi-stationary laser ablation fronts in strongly radiating plasmas. *Phys. Plasmas* **2015**, *22*, 053111. [[CrossRef](#)]
28. Basko, M. On the maximum conversion efficiency into the 13.5-nm extreme ultraviolet emission under a steady-state laser ablation of tin microspheres. *Phys. Plasmas* **2016**, *23*, 083114. [[CrossRef](#)]
29. Su, M.; Min, Q.; Cao, S.; Sun, D.; Hayden, P.; O’Sullivan, G.; Dong, C. Evolution analysis of EUV radiation from laser-produced tin plasmas based on a radiation hydrodynamics model. *Sci. Rep.* **2017**, *7*, 45212. [[CrossRef](#)] [[PubMed](#)]
30. Hemminga, D.J.; Poirier, L.; Basko, M.M.; Hoekstra, R.; Ubachs, W.; Versolato, O.O.; Sheil, J. High-energy ions from Nd:YAG laser ablation of tin microdroplets: Comparison between experiment and a single-fluid hydrodynamic model. *Plasma Sources Sci. Technol.* **2021**, *30*, 105006. [[CrossRef](#)]
31. Cummings, A.; O’Sullivan, G.; Dunne, P.; Sokell, E.; Murphy, N.; White, J. Conversion efficiency of a laser-produced Sn plasma at 13.5 nm, simulated with a one-dimensional hydrodynamic model and treated as a multi-component blackbody. *J. Phys. D Appl. Phys.* **2005**, *38*, 604–616. [[CrossRef](#)]
32. Sizyuk, V.; Hassanein, A.; Sizyuk, T. Three-dimensional simulation of laser-produced plasma for extreme ultraviolet lithography applications. *J. Appl. Phys.* **2006**, *100*, 103106. [[CrossRef](#)]
33. Sunahara, A.; Sasaki, A.; Nishihara, K. Two dimensional radiation hydrodynamic simulation for extreme ultra-violet emission from laser-produced tin plasmas. *J. Physics Conf. Ser.* **2008**, *112*, 042048. [[CrossRef](#)]
34. Purvis, M.A.; Schafgans, A.; Brown, D.J.W.; Fomenkov, I.; Rafac, R.; Brown, J.; Tao, Y.; Rokitski, S.; Abraham, M.; Vargas, M.; et al. Advancements in predictive plasma formation modeling. In Proceedings of the Extreme Ultraviolet (EUV) Lithography VII, Bellingham, WA, USA, 18 March 2016; Volume 9776, pp. 159–170.
35. Hassanein, A.; Sizyuk, T. Laser produced plasma sources for nanolithography—Recent integrated simulation and benchmarking. *Phys. Plasmas* **2013**, *20*, 053105. [[CrossRef](#)]
36. Masnavi, M.; Parchamy, H. Calculation of the extreme-ultraviolet radiation conversion efficiency for a laser-produced tin plasma source. *Phys. Open* **2019**, *1*, 100003. [[CrossRef](#)]
37. Mayer, P.; Brandt, D.C.; Fomenkov, I.; Purvis, M.; Brown, D. Laser produced plasma EUV sources for N5 HVM and beyond: Performance, availability and technology innovation. In Proceedings of the Extreme Ultraviolet (EUV) Lithography XII, Online Event, 22–25 February 2021; Volume 11609.
38. Sizyuk, T.; Hassanein, A. Tuning laser wavelength and pulse duration to improve the conversion efficiency and performance of EUV sources for nanolithography. *Phys. Plasmas* **2020**, *27*, 103507. [[CrossRef](#)]
39. Behnke, L.; Schupp, R.; Bouza, Z.; Bayraktar, M.; Mazzotta, Z.; Meijer, R.; Sheil, J.; Witte, S.; Ubachs, W.; Hoekstra, R.; et al. Extreme ultraviolet light from a tin plasma driven by a 2- $\mu\text{m}$ -wavelength laser. *Opt. Express* **2021**, *29*, 4475–4487. [[CrossRef](#)]
40. Tamer, I.; Reagan, B.A.; Galvin, T.; Galbraith, J.; Sistrunk, E.; Church, A.; Huete, G.; Neurath, H.; Spinka, T. Demonstration of a compact, multi-joule, diode-pumped Tm:YLF laser. *Opt. Lett.* **2021**, *46*, 5096–5099. [[CrossRef](#)]
41. Yuan, Y.; Ma, Y.Y.; Wang, W.P.; Chen, S.J.; Cui, Y.; Zi, M.; Yang, X.H.; Zhang, G.B.; Leng, Y.X. Enhancing the conversion efficiency of extreme ultraviolet light sources using a 2  $\mu\text{m}$  wavelength laser. *Plasma Phys. Control. Fusion* **2021**, *64*, 025001. [[CrossRef](#)]
42. Hemminga, D.J.; Versolato, O.O.; Sheil, J. Simulations of plasmas driven by laser wavelengths in the 1.064–10.6  $\mu\text{m}$  range for their characterization as future extreme ultraviolet light sources. *Phys. Plasmas* **2023**, *30*, 033301. [[CrossRef](#)]
43. Schupp, R.; Torretti, F.; Meijer, R.; Bayraktar, M.; Scheers, J.; Kurilovich, D.; Bayerle, A.; Eikema, K.; Witte, S.; Ubachs, W.; et al. Efficient Generation of Extreme Ultraviolet Light From Nd:YAG-Driven Microdroplet-Tin Plasma. *Phys. Rev. Appl.* **2019**, *12*, 014010. [[CrossRef](#)]
44. Lee, R.W.; Nash, J.; Ralchenko, Y. Review of the NLTE kinetics code workshop. *J. Quant. Spectrosc. Radiat. Transf.* **1997**, *58*, 737–742. [[CrossRef](#)]
45. Rubiano, J.; Florido, R.; Bowen, C.; Lee, R.; Ralchenko, Y. Review of the 4th NLTE Code Comparison Workshop. *High Energy Density Phys.* **2007**, *3*, 225–232. [[CrossRef](#)]
46. Fontes, C.; Abdallah, J.; Bowen, C.; Lee, R.; Ralchenko, Y. Review of the NLTE-5 kinetics workshop. *High Energy Density Phys.* **2009**, *5*, 15–22. [[CrossRef](#)]
47. Available online: <https://euvlitho.com/code-comparison/code-comparison-2020/> (accessed on 9 October 2023).

48. Hansen, S.; Chung, H.K.; Fontes, C.; Ralchenko, Y.; Scott, H.; Stambulchik, E. Review of the 10th Non-LTE code comparison workshop. *High Energy Density Phys.* **2020**, *35*, 100693. [[CrossRef](#)]
49. Sasaki, A.; Murakami, I. Validation of Collisional Radiative Model of High-Z Multiple Charged Ions at NLTE Code Comparison Workshops. *Plasma Fusion Res.* **2013**, *8*, 2401021. [[CrossRef](#)]
50. Magee, N.H.; Abdallah, J.; Colgan, J.; Hakel, P.; Kilcrease, D.P.; Mazevet, S.; Sherrill, M.; Fontes, C.J.; Zhang, H. Los Alamos opacities: Transition from LEDCOP to ATOMIC. *AIP Conf. Proc.* **2004**, *730*, 168–179.
51. Hakel, P.; Sherrill, M.E.; Mazevet, S.; Abdallah, J., Jr.; Colgan, J.; Kilcrease, D.P.; Magee, N.H.; Fontes, C.J.; Zhang, H.L. The new Los Alamos opacity code ATOMIC. *J. Quant. Spectrosc. Radiat. Transf.* **2006**, *99*, 265–271. [[CrossRef](#)]
52. Nikiforov, A.F.; Novikov, V.G.; Uvarov, V.B. *Quantum-Statistical Models of Hot Dense Matter: Methods for Computation Opacity and Equation of State*; Birkhäuser: Basel, Switzerland, 2006; Volume 37.
53. Vichev, I.; Solomyannaya, A.; Grushin, A.; Kim, D. On certain aspects of the THERMOS toolkit for modeling experiments. *High Energy Density Phys.* **2019**, *33*, 100713. [[CrossRef](#)]
54. MacFarlane, J.J.; Golovkin, I.E.; Woodruff, P.R.; Welch, D.R.; Oliver, B.V.; Mehlhorn, T.A.; Campbell, R.B. Simulation of the ionization dynamics of aluminium irradiated by intense short-pulse lasers. *Inert. Fus. Sci. Appl.* **2003**, 457.
55. Scott, H.A. Cretin—A radiative transfer capability for laboratory plasmas. *J. Quant. Spectrosc. Radiat. Transf.* **2001**, *71*, 689–701. [[CrossRef](#)]
56. Frank, Y.; Louzon, E.; Mandelbaum, P.; Henis, Z. SEMILLAC: A new hybrid atomic model of hot dense plasmas. *High Energy Density Phys.* **2013**, *9*, 594–600. [[CrossRef](#)]
57. Frank, Y.; Mandelbaum, P.; Henis, Z. SEMILLAC II: A new model for spectral behavior of hot plasmas. *High Energy Density Phys.* **2014**, *12*, 27–34. [[CrossRef](#)]
58. Sunahara, A.; Johzaki, T.; Nagatomo, H.; Mima, K. Generation of pre-formed plasma and its reduction for fast-ignition. *Laser Part. Beams* **2012**, *30*, 95–102. [[CrossRef](#)]
59. Sunahara, A. Development of Radiation Hydrodynamic code STAR for EUV plasmas. In Proceedings of the EUV Source Workshop, Dublin, Ireland, 3–7 November 2013.
60. Basko, M.M.; Maruhn, J.A.; Tauschwitz, A. Development of a 2D radiation-hydrodynamics code RALEF for laser plasma simulations. *GSI Rep.* **2010**, *1*, 410.
61. Basko, M.M.; Sasorov, P.V.; Murakami, M.; Novikov, V.G.; Grushin, A.S. One-dimensional study of the radiation-dominated implosion of a cylindrical tungsten plasma column. *Plasma Phys. Control. Fusion* **2012**, *54*, 055003. [[CrossRef](#)]
62. MacFarlane, J.J.; Golovkin, I.E.; Woodruff, P.R. HELIOS-CR—A 1-D radiation-magnetohydrodynamics code with inline atomic kinetics modeling. *J. Quant. Spectrosc. Radiat. Transf.* **2006**, *99*, 381–397. [[CrossRef](#)]
63. Torretti, F.; Liu, F.; Bayraktar, M.; Scheers, J.; Bouza, Z.; Ubachs, W.; Hoekstra, R.; Versolato, O. Spectral characterization of an industrial EUV light source for nanolithography. *J. Phys. D Appl. Phys.* **2019**, *53*, 055204. [[CrossRef](#)]
64. Chung, H.K.; Bowen, C.; Fontes, C.; Hansen, S.; Ralchenko, Y. Comparison and analysis of collisional-radiative models at the NLTE-7 workshop. *High Energy Density Phys.* **2013**, *9*, 645–652. [[CrossRef](#)]
65. Hansen, S. Balancing Detail and Completeness in Collisional-Radiative models. In *Modern Methods in Collisional-Radiative Modeling of Plasmas*; Ralchenko, Y., Ed.; Springer: Cham, Switzerland, 2016; pp. 1–15.
66. de Gaufridy de Dortan, F. Influence of configuration interaction on satellite lines of xenon and tin in the EUV region. *J. Phys. B* **2007**, *40*, 599–615. [[CrossRef](#)]
67. D’Arcy, R.; Ohashi, H.; Suda, S.; Tanuma, H.; Fujioka, S.; Nishimura, H.; Nishihara, K.; Suzuki, C.; Kato, T.; Koike, F.; et al. Transitions and the effects of configuration interaction in the spectra of Sn XV–Sn XVIII. *Phys. Rev. A* **2009**, *79*, 042509. [[CrossRef](#)]
68. Ohashi, H.; Suda, S.; Tanuma, H.; Fujioka, S.; Nishimura, H.; Sasaki, A.; Nishihara, K. EUV emission spectra in collisions of multiply charged Sn ions with He and Xe. *J. Phys. B At. Mol. Opt. Phys.* **2010**, *43*, 065204. [[CrossRef](#)]
69. D’Arcy, R.; Morris, O.; Ohashi, H.; Suda, S.; Tanuma, H.; Fujioka, S.; Nishimura, H.; Nishihara, K.; Suzuki, C.; Kato, T.; et al. Configuration interaction in charge exchange spectra of tin and xenon. *Phys. Scr.* **2011**, *T144*, 014026. [[CrossRef](#)]
70. Scheers, J.; Shah, C.; Ryabtsev, A.; Bekker, H.; Torretti, F.; Sheil, J.; Czapski, D.A.; Berengut, J.C.; Ubachs, W.; López-Urrutia, J.R.C.; et al. EUV spectroscopy of highly charged Sn<sup>13+</sup>–Sn<sup>15+</sup> ions in an electron-beam ion trap. *Phys. Rev. A* **2020**, *101*, 062511. [[CrossRef](#)]
71. Bouza, Z.; Scheers, J.; Ryabtsev, A.; Schupp, R.; Behnke, L.; Shah, C.; Sheil, J.; Bayraktar, M.; López-Urrutia, J.R.C.; Ubachs, W.; et al. EUV spectroscopy of Sn<sup>5+</sup>–Sn<sup>10+</sup> ions in an electron beam ion trap and laser-produced plasmas. *J. Phys. B At. Mol. Opt. Phys.* **2020**, *53*, 195001. [[CrossRef](#)]
72. Windberger, A.; Torretti, F.; Borschevsky, A.; Ryabtsev, A.; Dobrodey, S.; Bekker, H.; Eliav, E.; Kaldor, U.; Ubachs, W.; Hoekstra, R.; et al. Analysis of the fine structure of Sn<sup>11+</sup>–Sn<sup>14+</sup> ions by optical spectroscopy in an electron-beam ion trap. *Phys. Rev. A* **2016**, *94*, 012506. [[CrossRef](#)]
73. Filin, D.; Savukov, I.; Colgan, J. Relativistic Configuration-Interaction and Perturbation Theory Calculations of the Sn XV Emission Spectrum. *Atoms* **2021**, *9*, 96. [[CrossRef](#)]
74. Sasaki, A.; Nishihara, K.; Murakami, M.; Koike, F.; Kagawa, T.; Nishikawa, T.; Fujima, K.; Kawamura, T.; Furukawa, H. Effect of the satellite lines and opacity on the extreme ultraviolet emission from high-density Xe plasmas. *Appl. Phys. Lett.* **2004**, *85*, 5857–5859. [[CrossRef](#)]

75. Sheil, J.; Versolato, O.O.; Neukirch, A.J.; Colgan, J. Multiply-excited states and their contribution to opacity in CO<sub>2</sub> laser-driven tin-plasma conditions. *J. Phys. B At. Mol. Opt. Phys.* **2021**, *54*, 035002. [[CrossRef](#)]
76. Lee, Y.T.; More, R.M. An electron conductivity model for dense plasmas. *Phys. Fluids* **1984**, *27*, 1273–1286. [[CrossRef](#)]
77. Skupsky, S. “Coulomb logarithm” for inverse-bremsstrahlung laser absorption. *Phys. Rev. A* **1987**, *36*, 5701–5712. [[CrossRef](#)]
78. Scott, H.; Langer, S.; Frank, Y. Radiation-Hydrodynamics Modeling of LPP EUV Sources. In *Photon Sources for Lithography and Metrology*; Bakshi, V., Ed.; SPIE Press: Washington, DC, USA, 2023; pp. 71–110.

**Disclaimer/Publisher’s Note:** The statements, opinions and data contained in all publications are solely those of the individual author(s) and contributor(s) and not of MDPI and/or the editor(s). MDPI and/or the editor(s) disclaim responsibility for any injury to people or property resulting from any ideas, methods, instructions or products referred to in the content.